AIChE

Dispersed ZrO_2 Nanoparticles in MCM-48 with High Adsorption Activity

Parag A. Deshpande, Sneha Polisetti, and Giridhar Madras
Dept. of Chemical Engineering, Indian Institute of Science, Bangalore 560012, India

Divya Jyothi and Srinivasan Chandrasekaran
Dept. of Organic Chemistry, Indian Institute of Science, Bangalore 560012, India

DOI 10.1002/aic.13719
Published online January 4, 2012 in Wiley Online Library (wileyonlinelibrary.com).

A new two-step synthesis of ZrO_2-MCM nanocomposites using the gel combustion technique was accomplished; the resulting material had a high-surface area and showed very high adsorption activity. The deposition of 2–5 nm ZrO_2 particles over MCM was achieved using gel combustion technique with glycine as a fuel, and the formation of nanocomposites was confirmed using transmission electron microscopy. The composites were also characterized by XRD, SEM, FTIR and N_2 adsorption-desorption analysis. The nanocomposites were tested for the adsorption of cationic dyes. High rates of adsorption and large dye uptake were observed over the nanocomposites. The rate of adsorption over the nanocomposites was higher than that observed for physical ZrO_2-MCM mixtures and commercial activated carbon. The nanocomposite with 10 wt % ZrO_2 showed the highest rate of adsorption owing to the synergistic effects of ZrO_2 surface groups, smaller particle size, fine dispersion and high-surface area of the composite. © 2012 American Institute of Chemical Engineers *AIChE J*, 58: 2987–2996, 2012
Keywords: nanocomposites, ZrO_2-MCM, surface area, adsorption isotherms

Introduction

The concept of active species and support is well established in the literature of catalysis. Several techniques have been developed for obtaining a high dispersion of the active species in the support matrix. However, this can, in principle, be used for any operation requiring high mass-transfer rates. Thus, nanocomposites have been used in polymer technology,[1] ceramics,[2] biomedical engineering,[3] and nanotechnology.[4] Nanomaterials can be supported on porous materials having high surface area. Some of the common supports include noncrystalline mesostructured materials such as MCM-41/48. Mobil composition of matter (MCM) class of materials was reported Kresge et al.[5] as mesoporous and microporous inorganic solids, synthesized using liquid template technique. MCM compounds basically consist of SiO_2 network framework with amorphous structure. However, large local ordered structures are present in such compounds, generally as hexagonal or cubic arrangement, which can be observed using electron microscopic techniques. Various MCM compounds have been reported by several investigators with an aim of achieving compounds with high surface areas and controlled pore sizes. Different measures for the alteration of such characteristics have been found to be vital for application of the compounds as selective catalysts.[6–8] High surface area of such compounds also makes them suitable as adsorbents.[9–11] Nanocomposites of MCM with different metals and metal oxides have been reported for catalytic applications. B, Al, Ti, Co and Sn incorporated MCM composites have been synthesized using various techniques.[12–16]

Zirconium has been incorporated in the structure of MCM, as reported by Jiang et al.[17] and Chen et al.[18] A large number of studies report the use of different oxides in MCM. However, there are no reports describing a fine dispersion of ZrO_2 in MCM. We have recently reported[19] high rates and uptake of adsorption of cationic dyes over combustion synthesized ZrO_2 with a surface area of 12 m^2/g. This surface area is very low compared to that of typical commercial adsorbents. An enhancement in the adsorption activity can be expected with an increase in the surface area of the compound. To accomplish this, we adopted the strategy of synthesis of nanocomposites of ZrO_2 with high surface area MCM.

Nucleation and growth of particles on a substrate to obtain a fine dispersion of particles and restrict the particle dimension in nanometer range are important processes governing the final properties of the composite material. The grain boundary effects and dispersion of active species can have significant consequences on the properties and applicability of the material. However, the evolution of the composite is strongly dependent on the method of synthesis and the properties of the nanocomposite can be tailored by suitably adjusting the synthesis conditions. In this study, we have used a new technique based on gel combustion to obtain an extremely fine dispersion of ZrO_2 in the support MCM

Additional Supporting Information can be found in the online version of this article.

Correspondence concerning this article should be addressed to G. Madras at giridhar@chemeng.iisc.ernet.in.

matrix, where the ZrO_2 nanoparticles are nucleated over the surface of MCM during the synthesis. The technique harnesses the fact that rapid combustion and quenching of the flame along with the liberation of a large volume of gases result in restriction of the particle size to nanometer range. Although numerous efforts have been made for nucleating metal nanoparticles over high-surface area substrate using wet chemical methods, the novelty of this method is that it provides a rapid way of dispersing metal oxide nanoparticles. The key achievement of this technique is that a very fine dispersion of nanoparticles and non-segregation of the particles on the support can be obtained. To the best of our knowledge, this is the first study reporting the synthesis of ZrO_2-MCM nanocomposites synthesized by any technique. The composites showed superior activity for the adsorption of dyes when compared to bulk ZrO_2.

Experimental

Surfactant-assisted synthesis of MCM-48

Tetraethyl orthosilicate (TEOS, $Si(OC_2H_5)_4$, Merck, India) was used as the precursor for the synthesis of MCM-48. The surfactant used for the synthesis was cetyltrimethylammonium bromide (CTAB, $(C_{16}H_{33})N(CH_3)_3Br$, Merck, India). In a typical synthesis, 9.6 g of CTAB was added to 200 mL of deionized water and stirred vigorously. Furthermore, 200 mL of ethanol (de Commerce, Inc., Canada) and 60 mL of 25% ammonia solution (Merck, India) were added and solution was stirred. A clear solution was obtained after 10 min of stirring. 14.4 mL of TEOS was added to the clear solution with continuous stirring and a gel was observed to form. This reaction mixture was stirred for 2 h, filtered using Buchner funnel, and washed continuously with water. The solid formed was dried overnight at room temperature. Calcination of the dry solid was carried out at 550°C for 6 h. Bright white powder was obtained on calcination, referred to as MCM in the text.

Gel combustion synthesis of ZrO_2-MCM nanocomposites

ZrO_2-MCM nanocomposites were synthesized using a two-step process. MCM-48 was synthesized using the procedure described above. ZrO_2 nanoparticles were grown over MCM using gel combustion technique. ZrO_2 can be synthesized from zirconium nitrate and glycine using the solution combustion technique.[19] The reaction during combustion resulting in the formation of ZrO_2 is given as

$$10Zr(NO_3)_4 \cdot 5H_2O + 22C_2H_5NO_2 \rightarrow 10ZrO_2 + 31N_2 + 105H_2O + 44CO_2 + (1/2)O_2 \quad (1)$$

The aforementioned stoichiometry can also be arrived by balancing the oxidizing and reducing valences in the reaction mixture.[20] According to the aforementioned equation, every gram of zirconium nitrate results in the formation of 0.21 g of ZrO_2. The aforementioned stoichiometry was used for the synthesis of nanocomposites with different ZrO_2 wt % in MCM. In a typical synthesis of 10 wt % ZrO_2-MCM nanocomposite (ZM-10), 450 mg of MCM was taken. 238 mg of zirconium nitrate (Rolex, India) and 92 mg of glycine (Rolex, India) were added and the solids were finely ground in an agate mortar pestle to obtain a very fine powder. Two drops of water were added and the grinding was continued. A thick transparent gel was obtained on continuous grinding of the solids. The gel was carefully transferred to a crystallizing dish and the dish was placed in a muffle furnace. The temperature of the furnace was maintained at 350°C. The gel was observed to dehydrate and the formed solid was observed to protrude out of the dehydrated lump upon combustion. The voluminous solid mass formed was then finely ground and calcined at 500°C for 6 h and the calcined nanocomposite was bright white. Nanocomposites with 25 wt % (ZM-25), 50 wt % (ZM-50), and 75 wt % (ZM-75) of ZrO_2 were also synthesized by following the aforementioned procedure. The precursors and stoichiometric requirements for the synthesis of different nanocomposites are shown in Table 1.

Table 1. Precursors and Stoichiometry for Gel Combustion Synthesis of Different ZrO_2-MCM Nanocomposites

S. No.	Nanocomposite	MCM (mg)	zirconium nitrate (mg)	glycine (mg)
1	ZM-10	450	238	92
2	ZM-25	375	595	229
3	ZM-50	250	1190	458
4	ZM-75	125	1785	687

Characterization of the composites

Low-angle X-ray diffraction (XRD) was recorded on XD-D1 Shimadzu X-ray diffractometer. Wide-angle XRD was recorded on Phillips X'pert diffractometer with Cu Kα radiation and Ni filter. Scanning electron microscopy (SEM) images were recorded on Quanta 200 ESEM (FEI Quanta). The samples were coated with Pt and mounted on a conducting carbon tape. Transmission electron microscopy (TEM) images and electron diffraction patterns were recorded on Tecnai F-30 electron microscope with samples mounted on Cu-coated carbon grids. Infrared spectra were recorded on Jasco instrument. Thin pellets of the sample with KBr were made maintaining a composition of sample:KBr as 1:1 for all the samples. BET surface area was determined using Micromeritics ASAP 2020 apparatus with N_2 adsorption-desorption cycles. The synthesis of the composites was carried out in batches and similar characteristics were observed for different batches signifying the reproducibility of the method. The variation in the adsorption capacities of the material was less than 5% in different batches.

Dye adsorption experiments

The adsorption of cationic dyes over the nanocomposites was carried out in aqueous solutions. Methyl green (MG), brilliant green (BG), and malachite green (MCG) were chosen as model dyes for the analysis. Dye solutions of known concentrations were made and 50 mL of the dye solution was taken in a beaker. 20 mg of the adsorbent was added to the dye solution so as to maintain an adsorbent loading of 0.4 g/L. All the analysis for adsorption of the dye over the adsorbent, discussed later, was carried out on the basis of dye uptake "q" defined as the amount of dye adsorbed per unit mass of the adsorbent. This ensured that the results were independent of the amount of dye solution or adsorbent used. However, an adsorbent loading of 0.4 g/L, used consistently in all the experiments, minimized the experimental errors during the weighing of small amounts of solids. Samples were taken and centrifuged immediately to remove the suspended adsorbent particles. The finely ground solid used for the adsorption experiments had a particle size lesser than

200 μm. This ensured that the particles did not settle during the adsorption experiments. Centrifugation of the dye solution containing suspended particles for 90 s at 4,000 rpm resulted in separation of the suspended particles and a clear supernatant dye solution was obtained. The dye solution, free from suspended particles, was analyzed using a UV–vis spectrophotometer (Shimadzu 1700). All the experiments were carried out in dark to avoid the degradation of the dye due to photolysis. Further details on the experimental procedure can be found elsewhere.[19] All the experiments were repeated three times and the error bars in the determination of the adsorption rate constant and equilibrium concentrations are reported in the tables.

Results and Discussion

Characterization

Low-Angle X-ray Diffraction. The low-angle XRD pattern of MCM-48 is shown in Figure 1a. Several investigators have reported the XRD of MCM-48 cubic structure with characteristic 211, 220, 420 and 332 reflections in the range of 2–6°.[21–25] However, the lines in the current diffraction pattern were broad and the possibility of lamellar MCM-48 could not be discarded. Cubic and lamellar lines appear close in the XRD pattern, as reported by several investigators, for both pure phases and resolved mixed phases.[26–31] Whereas the appearance of the reflections indeed showed the formation of a long-range ordered compound, it was not possible to conclude the phase of the composites exclusively from the low-angle XRD analysis. Therefore, TEM analysis was carried out in order to confirm the phase of ZrO_2 and a detailed analysis of phase confirmation using TEM is provided in a later section.

Wide-angle X-ray diffraction

XRD patterns of all the composites were recorded in a 2θ range of 5–90° in order to determine the crystal structure of ZrO_2 that was crystallized over MCM during the synthesis of the nanocomposites. The XRD patterns of all the four nanocomposites are shown in Figure 1b. As can be seen from Figure 1b, no diffraction lines were observed for ZM-10 sample which contained 10 wt % of ZrO_2. Only the background pattern corresponding to the amorphous structure of MCM was observed. The absence of ZrO_2 diffraction lines in the sample indicated an extremely fine dispersion of ZrO_2 in MCM owing to which the diffraction corresponding to ZrO_2 was not visible. It is possible to obtain diffraction broad peaks for pure ZrO_2 with sub-10 nm crystallites. However, when nano-sized ZrO_2 is dispersed over a support in small quantities, the diffraction peaks may not appear due to the large background of the amorphous support. The nonobservance of the diffraction lines due to very high dispersion for both metals as well as metal oxides has been reported by several inveatigators.[32–34] However, the presence as well as the structure of ZrO_2, finely dispersed over MCM in ZM-10 nanocomposite was confirmed using TEM analysis and electron diffraction.

The samples with higher amounts of ZrO_2 showed diffraction lines corresponding to crystalline ZrO_2. This can be clearly seen in the various diffraction patterns in Figure 1b. The intensity of the peaks increased with ZrO_2 content, and all the characteristic peaks became observable at higher ZrO_2 loadings (ZM-75). The peaks were indexed to the tetragonal structure. The peaks for all the patterns were very broad and showed the formation of nanocrystallites. Although there are very small differences in the positions for the lines corresponding to cubic and tetragonal structures of ZrO_2, we have previously established the crystallization of ZrO_2 in the tetragonal phase using FT-Raman spectroscopy.[35] In this study, we have also used electron diffraction patterns for establishing the phase of ZrO_2 in the nanocomposites, as discussed later.

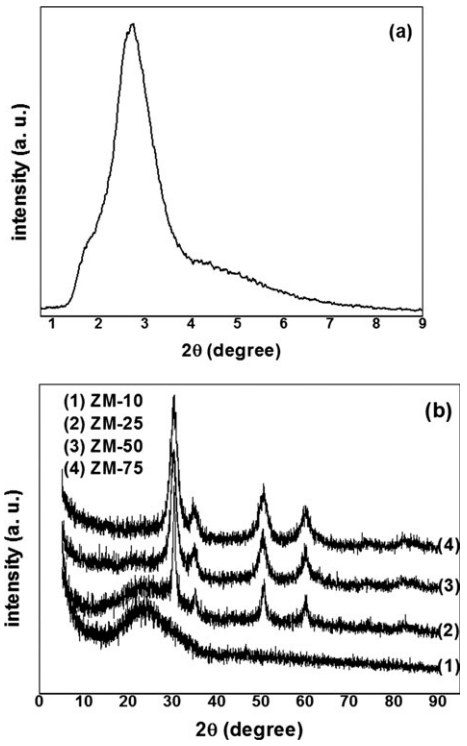

Figure 1. (a) Low-angle XRD of MCM-48, and (b) XRD patterns of the nanocomposites.

Scanning electron microscopy

The SEM micrographs of MCM-48 and ZM-50 are shown in Figure 2a and b, respectively. MCM-48 was observed to have spherical morphology, as seen in Figure 2a with particle sizes ranging from 100 to 500 nm. Spherical morphology of MCM-48 has also been observed by several investigators.[36–39] Unger and coworkers[36–38] have extensively studied MCM-48 systems, synthesized by different techniques and reported that spherical particles of sizes ranging from 200 to 1,000 nm were observed. Petitto et al.[39] have reported spherical MCM-48 particles of size of 10 μm. Using the surfactant-assisted synthesis reported in this study, it was possible to obtain spherical particles of smaller dimensions. Furthermore, the particles can be observed to be discrete and nonfused (Figure 2a and inset in the figure). No bulk agglomeration of the particles occurred even on post synthesis calcination treatment.

The SEM micrographs of ZM-50 sample in Figure 2b show the formation of uniform nanocomposite on a microscopic level. No segregation of MCM and ZrO_2 phases was observed and the composite consisted of a homogeneous structure when scanned through the different regions of the sample. The composite was found to be highly porous and the interconnected network of the pores can be seen in the figure. The morphology of the particles was observed to undergo small changes. The particles now attained a

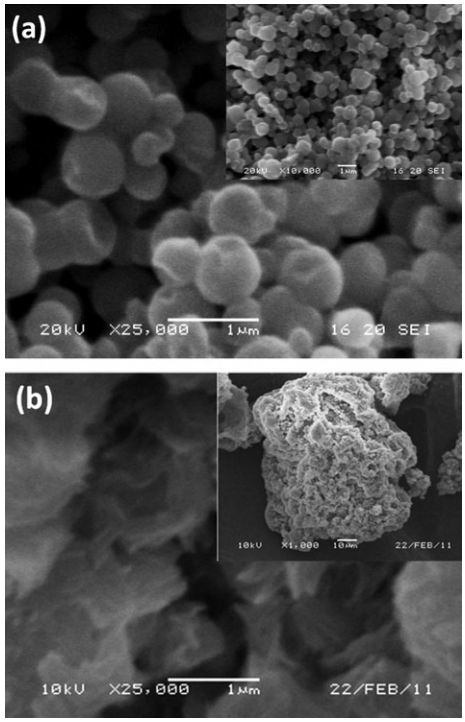

Figure 2. SEM images of (a) MCM-48, and (b) ZM-50.

distorted spherical shape (inset in the figure). We have previously observed highly porous ZrO_2 particles with flakelike morphology.[19] It is interesting to note that the flakelike morphology within the spherical particles can indeed be observed and the nanocomposite possessed the characteristic of both MCM as well as ZrO_2. Schumacher et al.[36] have observed that spherical morphology was obtained by room temperature methods only. Therefore, the change in the morphology of the nanocomposite in the current study can be attributed to the thermal treatment of the compound during the gel combustion.

Transmission electron microscopy

The TEM image of MCM-48 is shown in Figure 3a. The image suggests the crystallization of MCM mostly in the lamellar structure. Two-dimensional (2-D) layered structures can be observed in the image. Furthermore, the ordered cubic or hexagonal arrangements, characteristic of the cubic or hexagonal structure, were absent. This confirmed that MCM did not crystallize in cubic structure and retained the layered structure.

TEM analysis was further carried out for nanocomposites for structural analysis and for the confirmation of the formation of nanocomposites. Therefore, TEM images for ZM-10 as well as ZM-50 were recorded. The lamellar structure of MCM in the nanocomposite can be observed in the images for ZM-10 (Figure 3b). ZrO_2 particles can be clearly observed in the images and a very fine dispersion of ZrO_2 was achieved. It is also interesting to note that the electron diffraction pattern showed the diffraction rings confirming the presence of ZrO_2 particles. These rings were not observed in the diffraction pattern of MCM. Furthermore, the XRD of ZM-10 could not capture the presence of ZrO_2 particles. Therefore, it can be concluded from the TEM image analysis and electron diffraction that a very fine dispersion of ZrO_2 in MCM was indeed achieved. EDS analysis also confirmed the presence of ZrO_2 in the composite (see additional supporting information for Figure S1).

The particle size in case of ZM-50 increased, as can be seen from Figure 3c. ZrO_2 particles of an average size of 5

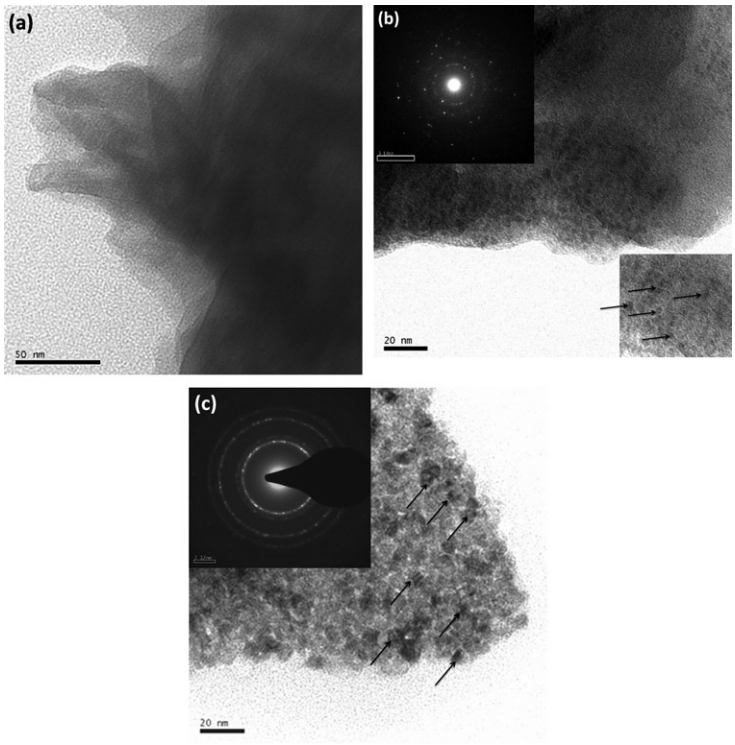

Figure 3. TEM images of (a) MCM-48, (b) ZM-10, and (c) ZM-50.

Electron diffraction patterns for the nanocomposites are shown in insets.

nm can be observed in the images. Similar to the observation from the SEM analysis, it can be observed in the TEM images also that the particles were dispersed in the support MCM and segregated agglomerates of ZrO_2 and MCM were not observed. This confirmed that the compound was indeed a nanocomposite in which ZrO_2 was nucleated and grown over MCM with the particles adhering strongly to the surface, thus, making it different from a physical mixture. Electron diffraction pattern for the nanocomposite can also be seen in the figure confirming the formation of ZrO_2.

FT-infrared spectroscopy

The FTIR spectra of MCM-48, ZrO_2-MCM nanocomposites and ZrO_2 are shown in Figure S2 (see supporting information). The spectrum of Figure S2a is a typical IR spectrum for MCM class of compounds reported by several investigators.[15–16,40–44] Peaks were observed at 467, 800, 970, 1,080, 1,240, 1,590–1,630 and 3,460 cm^{-1}. The presence of a broad band at 3,460 cm^{-1} can be attributed to adsorbed water molecules and Si-OH stretching vibrations. The peaks at 467 and 800 cm^{-1} were due to symmetric Si-O stretching vibrations and tetrahedral Si-O bending. The peak at 970 cm^{-1} was present due to symmetric stretching vibrations of silanol Si-OH groups. The asymmetric Si-O-Si vibrations resulted in the appearance of the peaks at 1,080 and 1240 cm^{-1}. Bending modes of adsorbed water gave rise to the band at 1,590–1,630 cm^{-1}.

We have previously reported in detail the IR spectra for combustion synthesized ZrO_2[19] and the spectrum is shown in Figure S2f (see supporting information). We very briefly describe the main features of the spectra. A large band at 3,460 cm^{-1} can be observed in the spectra. All the spectra in Figure S2 were recorded maintaining the same concentration of composite in the sample and the background was subtracted for all the spectra. Therefore, it can be clearly seen from Figure S2 that OH groups were also present in ZrO_2, as signified by the band at 3,460 cm^{-1}. The peak at 1,650 cm^{-1} can be attributed both to the deformational vibrations of water as well as to stretching vibrations of C=C groups. The groups corresponding to carbon show their presence due to the fuel used in the synthesis of the composites. A wide peak in the range of 1,200–1,400 cm^{-1} was attributed to the presence of metal bound hydroxyl groups (Zr-OH). Therefore, ZrO_2 contained groups that were active for the adsorption of charged species such as dyes in solution. Furthermore, the mode of synthesis, i.e., combustion in the presence of a solid fuel, further resulted in the formation of partially charged carbon-based species (C=C, C=O, C—OH), which assisted in adsorption of cationic dyes.

The spectra for the nanocomposites are shown in Figure S2b–e. It can be observed in the spectra that surface hydroxyl group band (3,460 cm^{-1}) intensifies whenever both MCM as well as ZrO_2 are present. This can be clearly seen in the spectra of ZM-25 and ZM-50 (Figure S2b,c). This shows that the formation of nanocomposites results in the synergistic effect leading to a higher capacity of the composite to retain OH groups. Another important observation from the spectra is a large increase in the intensity for the peak at 980 cm^{-1}. As mentioned earlier, this corresponds to symmetric stretching vibrations of Si-OH groups. This is especially remarkable for ZM-10 nanocomposite, although the effect is observed in ZM-25 and ZM-50 also. Therefore, a large increase in the surface hydroxyl groups can be observed with the formation of nanocomposites. This is important from the point of view of applicability of the material for adsorption applications. Whereas individually both ZrO_2 as well MCM possessed different groups, the IR spectra revealed the synergism for retaining the surface groups in the nanocomposites where the contribution of ZrO_2 in MCM can clearly be observed for ZM-10 nanocomposite even when ZrO_2 was present only 10 wt %.

Surface area analysis

MCM synthesized in this study was a high surface area compound with a surface area of 1,090 m^2/g. Therefore, the compound was found to be suitable as a high surface area support for the dispersion of ZrO_2 nanoparticles. The surface area of ZM-10, ZM-25, ZM-50 and ZM-75 nanocomposites were found to be 183, 222, 251 and 306 m^2/g, respectively. All these surface areas were considerably higher compared to the surface area (12 m^2/g) of ZrO_2. Therefore, the aim of dispersion of ZrO_2 so as to obtain high surface area composite was indeed achieved.

Adsorption of dyes

The adsorption of all the dyes was first tested over MCM without ZrO_2 loading. Less than 20% adsorption of the dyes was observed in 2 h. ZM-50 was then tested for the adsorption of the dyes. The variation of normalized dye concentration for the different dyes with an initial dye concentration of 50 ppm and adsorbent loading of 0.4 g/L is shown in Figure 4. The adsorption of all the three dyes can be clearly seen in Figure 4. More than 60% adsorption of MG took place within first 5 min. A residual dye concentration of 1 ppm was observed after 1 h. The rates of adsorption were similar for BG and MCG. However, these rates were smaller than the rate of adsorption of MG. Nearly 35% adsorption was observed in 5 min and more than 80% adsorption was observed in 2 h. A detailed discussion of the mechanism of adsorption of dyes on ZrO_2 and the influence of the charged groups on adsorption has been discussed in our previous study.[19]

Having established the activity of ZM-50 for the adsorption of a number of dyes, further analysis was carried out for the adsorption of MG only. Further analysis can be carried out with range of dyes and establish the effect of the

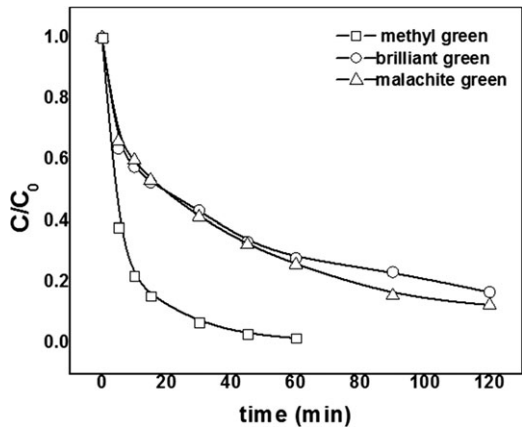

Figure 4. Variation of normalized dye concentration with time for various dyes during adsorption over ZM-50 with an initial dye concentration of 50 ppm and adsorbent loading of 0.4 g/L.

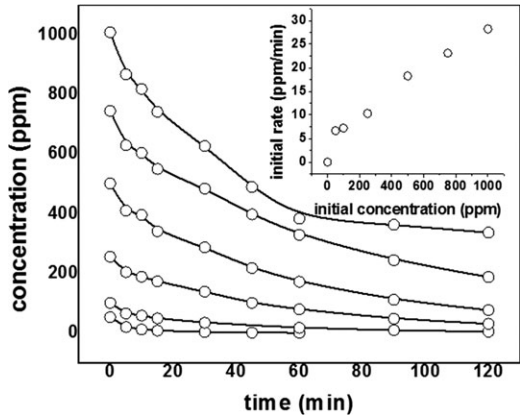

Figure 5. Variation of MG concentration with time during adsorption over ZM-50 with different initial dye concentrations with an adsorbent loading of 0.4 g/L.

The inset shows the effect of initial concentration of the dye on the initial rate of adsorption.

class and structure of the dye on adsorption. Experiments were carried out with different initial MG concentration keeping the adsorbent loading constant at 0.4 mg/L. The variation of the dye concentration with time is shown in Figure 5. The initial rate of adsorption (shown in inset of Figure 5) was found to increase with an increase in the initial dye concentration. A residual dye concentration of 5 ppm was observed after 2 h when an initial concentration of 100 ppm was used. Similarly, experiments were carried out with initial dye concentrations of 250 ppm, 500 ppm, 750 ppm and 1,000 ppm. With an increase in the initial concentration of the dye, an increase in the residual dye concentration in the solution was observed. A residual concentration of 337 ppm was observed at the end of 2 h with less than 2 ppm decrease in the concentration in the last 1 h when 1,000 ppm initial concentration was used. Equilibrium was also observed for other high concentrations when adsorption was carried out for a longer time. This is discussed later under isotherm analysis.

The effect of adsorbent loading on the adsorption of MG is shown in Figure 6 with an initial dye concentration of 50 ppm. The rate of adsorption was found to increase with an increase in adsorbent loading (inset of Figure 6). Whereas nearly 35% adsorption was observed with an adsorbent loading of 0.2 g/L, more than 75% adsorption was observed with an adsorbent loading of 0.6 g/L, 85% with 0.8 g/L, 92% with 1 g/L and nearly 98% with 2 g/L in 5 min. Saturation in the initial rate of adsorption was observed with an increase in the adsorbent loading, as can be seen from the inset in Figure 6.

The variation of normalized MG concentration with time over the different nanocomposites is shown in Figure 7a–d. A plot showing the variation of the initial rates of adsorption with % ZrO_2 for both nanocomposites as well as physical mixtures can be found online in supporting information (Figure S3). An initial dye concentration of 50 ppm and adsorbent loading of 0.4 g/L was used. Experiments with the same conditions were carried out for adsorption with pure ZrO_2 and commercial activated carbon also (Figure 7e). It is clear from the figures that ZM-10 nanocomposite showed the highest activity for the adsorption of MG in 5 min with nearly 80% adsorption and a residual dye concentration of less than 1 ppm in 30 min (Figure 7a). However, a sharp decrease in the rate of adsorption of the nanocomposites was observed on increasing ZrO_2 content to 25% by wt (Figure 7b). Nearly 60% decrease in the concentration was observed in 5 min, and a residual concentration of 5 ppm was observed after 60 min. The trend however reversed on increasing the amount of ZrO_2 with the rate of adsorption of ZM-50 being higher than that over ZM-25, and the rate of adsorption over ZM-75 being higher than that of ZM-50. A decrease in the rate of adsorption was observed when pure ZrO_2 was used (Figure 7e). It can be seen that the rate of adsorption of pure ZrO_2 was higher than that of the commercial activated carbon (Figure 7e), but lesser than the rate of adsorption of the composite. Furthermore, the rates of adsorption of MG by the physical mixtures of ZrO_2 and MCM were always lesser than the adsorption activity of the corresponding nanocomposites. The reasons behind these trends and the differences in the adsorption activity are explained with the help of adsorption kinetics discussed in the following section.

Kinetics of adsorption

The kinetics of adsorption of dyes over the adsorbents can be described as *n*th order process given by the following equation[45,46]

$$\frac{dC(t)}{dt} = k_n\{C(t) - C_e\}^n \tag{2}$$

We have found adsorption of MG over ZrO_2 to follow first kinetics ($n = 1$ in Eq. 2) in our previous study.[19] In this study also, the experimental observations could be satisfactorily described using the first-order kinetics. The continuous lines in Figure 7 show the variation of normalized dye concentration with time following first-order kinetics. Table 2 shows the first-order rate parameters and the equilibrium concentrations for the different composites. The rate of adsorption of the dyes over different composite followed the trend ZM-10 > ZM-75 > ZrO_2 > ZM-50 > ZM-25 > activated carbon.

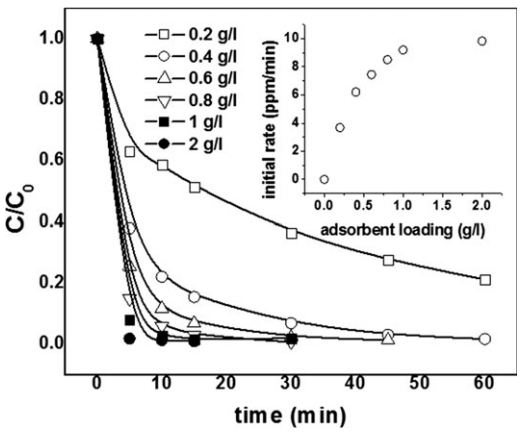

Figure 6. Variation of normalized MG concentration with time during adsorption over ZM-50, with different adsorbent loading with an initial dye concentration of 50 ppm.

The inset shows the effect of adsorbent loading of the initial rate of adsorption.

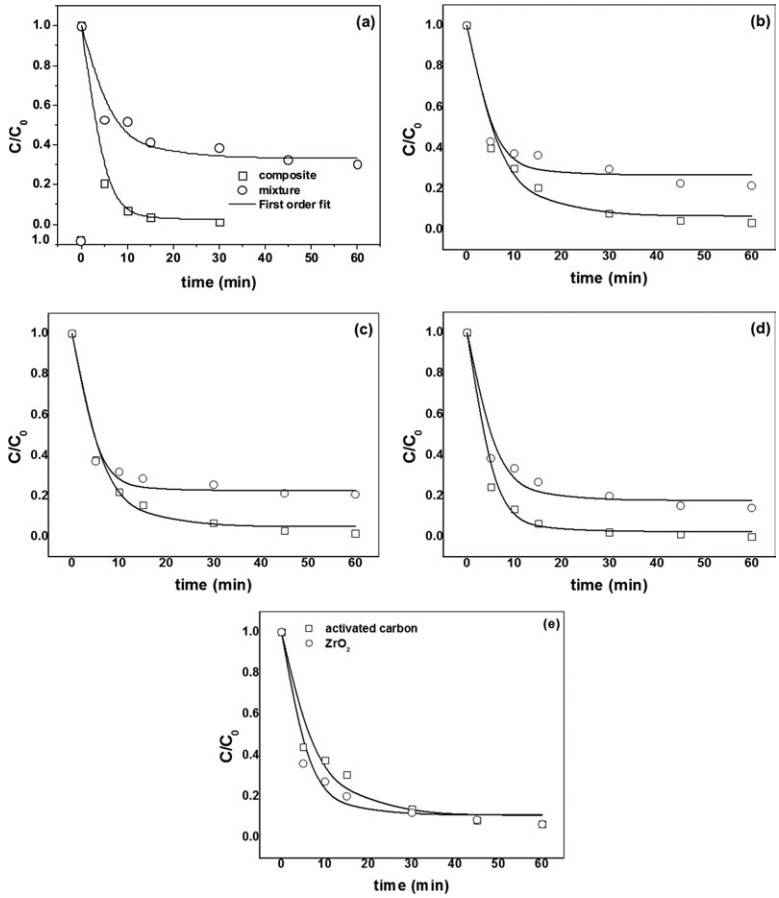

Figure 7. Variation of normalized MG concentration with time with (a) 10% ZrO_2, (b) 25% ZrO_2, (c) 50% ZrO_2, (d) 75% ZrO_2, and (e) combustion synthesized ZrO_2 and activated carbon.

The initial concentration of dye was 50 ppm and the adsorbent loading was 0.4 g/L. The points represent experimental data and the lines are based on first-order kinetics.

The aforementioned kinetic parameters can be used for comparing the relative rates of adsorption over the different compounds. Two discontinuities occur in the aforementioned sequence that is different from the expected trend. First, there occurs a decrease in the activity of the composite with an increase in ZrO_2 weight from 10 to 25%. The rate of adsorption then increases monotonously with an increase in ZrO_2 content till 75% and reduces again for pure ZrO_2. We explain the aforementioned trend on the basis of surface groups, surface area and particle-size analysis.

Table 2. Predicted First-Order Rate Constant and Equilibrium Concentration for the Adsorption of MG over Different Composites

S. No.	Composite	Parameter		R^2
		C_e in ppm; k in min^{-1}		
1	ZM-10	k	0.33 ± 0.01	0.999
		C_e	1.1 ± 0.3	
2	ZM-10 Mix	k	0.17 ± 0.04	0.939
		C_e	16.7 ± 1.9	
3	ZM-25	k	0.16 ± 0.02	0.979
		C_e	3.4 ± 1.5	
4	ZM-25 Mix	k	0.25 ± 0.06	0.959
		C_e	13.4 ± 1.6	
5	ZM-50	k	0.19 ± 0.02	0.991
		C_e	2.6 ± 1.0	
6	ZM-50 Mix	k	0.30 ± 0.07	0.97
		C_e	11.4 ± 1.4	
7	ZM-75	k	0.28 ± 0.02	0.994
		C_e	1.3 ± 0.75	
8	ZM-75 Mix	k	0.22 ± 0.04	0.967
		C_e	9.0 ± 1.6	
9	ZrO_2	k	0.21 ± 0.03	0.981
		C_e	5.3 ± 1.3	
10	Activated carbon	k	0.14 ± 0.03	0.96
		C_e	5.4 ± 2.1	

The observed rate of adsorption of the dye over the composite is not merely a function of the surface area of the composite. This is apparent from our previous study where even low surface area ZrO_2 showed high activity for adsorption due to the presence of surface functional groups. Adsorption is also function of the total amount of ZrO_2 in the nanocomposite and the total amount of surface groups. In the previous study,[19] we have shown the influence of various surface groups on adsorption using spectroscopic techniques. With an increase in the amount of ZrO_2, a monotonous increase in the rate of adsorption is obtained for the composites with comparable surface areas. Similarly, an increase in the rate of adsorption is expected with an increase in the surface area of the composites.

The composites synthesized in this study showed widely different surface areas. Hence, both the surface area and the amount of ZrO_2 increase from ZM-10 to ZM-75. This trend is indeed followed for ZM-25, ZM-50 and ZM-75, with the rate of adsorption of ZM-75 being the highest and the rate of adsorption of ZM-25 being the lowest. However, a high rate of adsorption of ZM-10 is observed and,

therefore, it is important to consider the surface functional groups.

As mentioned previously, ZM-10 was observed to have a high accumulation of surface groups and this can be a possible reason behind the high rate of adsorption of dye over this composite. The surface area of this composite was 15 times higher than the surface area of ZrO_2. The dispersion of ZrO_2 in MCM was very fine as the particle size was as small as 2 nm. Therefore, high-surface area and accumulation of a large amount of active surface groups resulted in imparting a high adsorption activity to the composite. The rate of adsorption of ZrO_2 was found to be lesser than the rate of adsorption of ZM-75. This clearly shows the relative importance of the amount of ZrO_2 and the surface area of the composite for adsorption. The surface area of ZM-75 was 25 times higher than the surface area of ZrO_2. Whereas the amount of ZrO_2in ZM-75 was ¾th amount in pure ZrO_2, the increase in the rate was nearly 35% against 57% for ZM-10. Therefore, from the aforementioned trend, it can be concluded that no simple relation exists between the various factors affecting the adsorption and since the different factors influencing the rates of adsorption can be inter-related and synergistic effects have to be considered to explain the behavior of the composites.

The earlier arguments can further be rationalized with the help of observations from the experiments with physical mixtures of MCM and ZrO_2. In case of physical mixtures, the trend for rate of adsorption, signified by first-order rate constant (Table 2), was ZM-50 > ZM-25 > ZM-75 > ZrO_2 > ZM-10. The activity of the composite goes through a maximum as a function of ZrO_2 weight with the maximum rate of adsorption observed for ZM-50. Therefore, it can be said that the rate of adsorption increased with an increase in the amount of ZrO_2. However, at very high ZrO_2 concentrations, the surface area of the mixture decreased and as a result, a decrease in the rate of adsorption of the dye was observed.

Apart from the differences in the rate of adsorption of the composites and mixtures, another interesting observation was the difference in the equilibrium concentrations. With mixtures, large residual equilibrium dye concentrations were observed. When a fine physical mixture of MCM and ZrO_2 was introduced in the dye solutions, dispersion of ZrO_2 indeed took place resulting in rate of adsorption of the dyes which was higher than that of pure ZrO_2. Higher rate of adsorption with lower ZrO_2 amounts clearly showed the dispersion effects and enhancement in surface area even with the physical mixture. However, the concentrations with physical mixtures were found to quickly saturate showing equilibrium adsorption. Since ZrO_2 was not nucleated over MCM, separation of ZrO_2 and MCM components of the mixture took place in aqueous medium over time in the presence of constant stirring. Since ZrO_2 was the only active component in the composite and a decrease in both the amount as well as surface area took place due to separation, the rate of adsorption of the dye over the composite remained essentially the same as that of pure ZrO_2. In the range of ZrO_2 concentrations used in this study, a monotonous increase in the adsorption capacity is observed with adsorbent amount.[19] Therefore; the physical mixtures do not retain the advantage of dispersion after a certain interval of time. This was not the case for the nanocomposites synthesized in this study which not only showed high activity for adsorption, but also showed large dye uptake at equilibrium. Although the surface area of a compound can be controlled, altering the surface groups and their concentration is difficult and requires post processing of the adsorbents. In this study, we have been able to demonstrate a method of rapid synthesis of the adsorbents with improved adsorption characteristics and have not attempted to examine the influence of surface area and surface groups individually.

Isotherm analysis

We present the isotherm analysis for the adsorption of MG over the nanocomposites. A number of adsorption isotherms have been described and these have been derived using different assumptions and, therefore, the parameters appearing in the isotherms signify different physical quantities. An excellent overview of different isotherms along with the kinetic analysis can be found in a recent work by Duran et al.[47] We have analyzed four different isotherms and the associated parameters for the adsorption of MG is shown in Figure 3.

Figure 8 shows the variation of equilibrium dye uptake with equilibrium dye concentration in solution over ZM-50 and ZrO_2 at 25°C. The experiments were carried out with different initial MG concentrations and the experiments depicted in Figure 5 were extended for 24 h. Samples were taken every hour after 12 h to ensure that equilibrium was attained. Similarly, experiments were conducted with pure ZrO_2 and these experiments were similar to that reported in our previous study.[19] It was established in that study[19] that the equilibrium adsorption capacity of ZrO_2 was slightly higher than that of commercial activated carbon. The rate of adsorption of pure ZrO_2 was also higher than that of the commercial activated carbon (Figure 7e), but lesser than the rate of adsorption over the composite. In order to model the equilibrium dye uptake, correlations were carried out using various isotherms.

Langmuir Isotherm

Langmuir isotherm[47–49] assumes monolayer adsorption of the adsorbent over energetically uniform adsorbate, and is given by

$$q_e = \frac{q_m k_l C_e}{1 + k_l C_e} \tag{4}$$

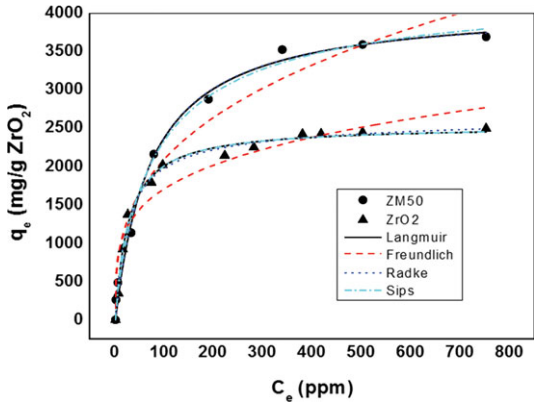

Figure 8. Adsorption isotherms showing the variation of the equilibrium dye uptake with equilibrium dye concentration for the adsorption of MG.

The points represent experimental data and the lines are based on correlations by different isotherms. [Color figure can be viewed in the online issue, which is available at wileyonlinelibrary.com.]

Table 3. Isotherm Parameters for the Adsorption of MG over ZrO_2 and ZM-50

Isotherm	Parameter	ZM-50	ZrO_2
Langmuir	q_m	4119 ± 134	2540 ± 43
	k_l	0.014 ± 0.002	0.038 ± 0.003
	R^2	0.991	0.991
Freundlich	k_f	456 ± 113	571 ± 109
	n_f	3.01 ± 0.39	4.19 ± 0.6
	R^2	0.960	0.925
Sips	q_m	4395 ± 372	2540 ± 79
	k_{lf}	0.022 ± 0.009	0.038 ± 0.01
	n_{lf}	0.86 ± 0.13	0.99 ± 0.11
	R^2	0.991	0.991
Radke-Prausnitz	q_m	4318 ± 245	2139 ± 427
	k_2	0.012 ± 0.03	0.05 ± 0.01
	β	1.0 ± 0.09	0.97 ± 0.03
	R^2	0.991	0.991

The isotherm describes the adsorption process fairly well, as signified by the reliability parameters for the fit of the data. The value of q_m gives the theoretical monolayer saturation capacity.[47–49]

Freundlich Isotherm. Freundlich isotherm is an empirical relation between the equilibrium dye uptake and equilibrium dye concentration and was proposed to account for the surface heterogeneity and is given as[47,48]

$$q_e = k_f C_e^{1/n} \tag{5}$$

The parameter n in the equation signifies the heterogeneity and is found be 3.01 for ZM-50 and 4.19 for ZrO_2. The fitting of the isotherm for the data was not satisfactory at higher equilibrium concentration. While it underpredicted the uptake at intermediate equilibrium concentrations, it overpredicted the uptake at very high-equilibrium concentrations.

Sips Isotherm. A composite isotherm, such as the Sips isotherm,[48,49] also known as the Langmuir-Freundlich isotherm is often used to describe adsorption, whose expression is given by

$$q_e = \frac{q_m k_{lf} C_e^{n_{lf}}}{1 + k_{lf} C_e^{n_{lf}}} \tag{6}$$

The isotherm reduces to Langmuir isotherm for $n_{lf} = 1$ and to Freundlich isotherm at low concentrations.

Radke-Prausnitz Isotherm. Radke-Prauznitz isotherm is a three-parameter model given as[49]

$$q_e = \frac{q_m k_2 C_e}{1 + k_2 C_e^{\beta}} \tag{7}$$

The isotherm reduces to Langmuir isotherm for $\beta = 1$ and reduces to Henry's law at infinite dilution. From reliability parameters, this isotherm could describe the equilibrium as well as the Sips isotherm.

The symbols in Figure 8 show the experimental data and the continuous lines show the predictions of the corresponding isotherm. The parameters obtained by nonlinear regression for all the isotherms are given in Table 3. From the figure, it is clear that the Langmuir isotherm correlates the experimental data well and is much superior to the correlation obtained by the Freundlich isotherm. The value of n_{lf} in the Sips isotherm and the value of β in the Radke-Prausnitz isotherm is close to unity indicating that the Langmuir isotherm is sufficient for correlating the experimental data and the three-parameter isotherms are not required. This is confirmed by the value of the correlation coefficient, whose value is 0.991 for all the three isotherms, namely Langmuir, Sips and Radke-Prausnitz isotherm. The value of q_m (indicating the equilibrium uptake) is around 4,100 mg/g for ZM-50 and around 2,500 mg/g for ZrO_2 (Table 3). This indicates that the adsorption activity of nanocomposites is superior to ZrO_2.

Conclusions

A very fine dispersion of ZrO_2 nanoparticles over high surface area MCM-48 was obtained using the gel combustion technique. The rate of adsorption of the nanocomposites formed by nucleation of ZrO_2 nanoparticles for the adsorption of cationic dyes was greatly enhanced when compared to the rate of adsorption over ZrO_2 alone. A number of factors contribute to this effect including surface area, particle size and amount of surface groups present in the nanocomposite. The higher adsorption capacity of the nanocomposites was due to strong adherence of ZrO_2 nanoparticles over the high surface area MCM, and this was found be significantly higher than the adsorption capacity observed with ZrO_2.

Literature Cited

1. Nayak SK, Mohanty S, Samal SK. Mechanical and thermal properties enhancement of polycarbonate nanocomposites prepared by melt compounding. *J Appl Polym Sci*. 2010;117:2101–2112.
2. Nair P, Mizukami F, Okubo T, Nair J, Keizer K, Burggraaf AJ. High-temperature catalyst supports and ceramic membranes: Metastability and particle packing. *AIChE J*. 1997;43:2710–2714.
3. Kretlow JD, Mikos AG. From materials to tissues: Biomaterial development, scaffold fabrication, and tissue engineering. *AIChE J*. 2008;12:3048–3067.
4. Liu J, Qiao SZ, Hu QH, Lu GQ. Magnetic nanocomposites with mesoporous structures: Synthesis and applications. *Small* 2011;4:425–443.
5. Kresge CT, Leonowicz ME, Roth WJ, Vartuli JC, Beck JS. Ordered mesoporous molecular sieves synthesized by a liquid-crystal template mechanism. *Nature* 1992;359, 710–712.
6. Sayari A. Catalysis by crystalline mesoporous molecular sieves. *Chem Mater*. 1996;8:1840–1852.
7. Brunel D, Blanc AC, Galarnearu A, Fajula F. New trends in the design of supported catalysts on mesoporous silicas and their applications to fine chemicals. *Catal Today*. 2002;73:139–152.
8. Ciesla U, Schuth F. Ordered mesoporous materials. *Microp Mesop Mater*. 1999;27:131–149.
9. Tian R, Zhang H, Ye M, Jiang X, Hu L, Li X, Bao X, Zou H. Selective extraction of peptides from human plasma by highly ordered mesoporous silica particles for pepridome analysis. *Angew Chemie Int Ed*. 2007;46:962–965.
10. Kim S, Ida J, Guliants VV, Lin JYS. Tailoring pore properties of MCM-48 silica for selective adsorption of CO_2. *J Phys Chem B*. 2005;109:6287–6293.
11. Moller K, Bein T. Inclusion chemistry in periodic mesoporous hosts. *Chem Mater*. 1998;10:2950–2963.
12. Zhang J, Liu M, Song C, Guo X. Facile synthesis of B-MCM-41 with controlled morphologies using water-acetone media. *Microp Mesop Mater*. 2011;139:31–37.
13. Zhao D, Budhi S, Rodriguez A, Koodali RT. Rapid and facile synthesis of Ti-MCM-48 mesoporous material and the photocatalytic performance for hydrogen evolution. *Int J Hydrogen Energy*. 2010;35:5276–5283.
14. Eimer GA, Pierella LB, Monti GA, Anunziata OA. Synthesis and characterization of Al-MCM-41 and Al-MCM-48 mesoporous materials. *Catal Lett*. 2002;78:65–75.
15. Zhao Q, Zhou X, Ji M, Ding H, Jiang T, Li C, Yin H. Stability and structural properties of cobalt incorporated MCM-48 mesoporous molecular sieve. *Appl Surf Sci*. 2011;257:2436–2442.

16. Sisodiya S, Shylesh S, Singh AP. Tin incorporated periodic mesoporous organisilicas (Sn-PMOs): Synthesis, characterization, and catalytic activity in the epoxidation reaction of olefins. *Catal Commun*. 2011;12:629–633.
17. Jiang T, Wu D, Song J, Zhau X, Zhao Q, Ji M, Yin H. Synthesis and characterization of mesoporous ZrMCM-48 molecular sieves with good thermal and hydrothermal stability. *Powder Technol*. 2011;207:422–427.
18. Chen L, Zhou X, Norena L, Wang J, Navarrete J, Salas P, Montoya A, Delangel P, Llanos M. Comparative studies of Zr-based MCM-41 and MCM-48 mesoporous molecular sieves: Synthesis and physicochemical properties. *Appl Surf Sci*. 2006;253:2443–2451.
19. Deshpande PA, Polisetti S, Madras G. Rapid synthesis of ultrahigh adsorption capacity zirconia by a solution combustion technique. *Langmuir* 2011;27:3578–3587.
20. Hegde MS, Madras G, Patil KC, Noble Metal Ionic Catalysts. *Accounts Chem. Res*. 2009;42:704–712.
21. Longloilert R, Chaisuwan T, Luengnaruemitchai A, Wongkasemjit S. Synthesis of MCM-48 from silatrane via sol-gel process. *J Sol-gel Sci Technol*. 2011;58:427–435.
22. Kruk M, Laroniec M, Pena ML, Rey F. Determination of phase composition of MCM-48/lamellar phase mixtures using nitrogen adsorption and thermogravimetry. *Chem Mater*. 2002;14:4434–4442.
23. Kim T-W, Chung P-W, Lin VS-Y. Facile synthesis of monodisperse sperical MCM-48 mesoporous silica nanoparticles with controlled particle size. *Chem Mater*. 2010;22:5093–5104.
24. Guan NC, Nur H, Endud S. Bimodal pore size mesoporous MCM-48 prepared by post-synthesis alumination. *J Phys Sci*. 2006;17:65–75.
25. Tkachenko OP, Klementiev KV, Loffler E, Ritzkopf I, Schüth F, Bandyopadhyay M, Grabowski S, Gies H, Hagen V, Muhler M, Lianhai L, Fischer RA, Grünert W. The structure of zinc and copper oxide species hosted in porous siliceous matrices. *Phys Chem Chem Phys*. 2003;5:4325–4334.
26. Zhao D, Goldfarb. Synthesis of mesoporous manganatosilicates: Mn-MCM-41, Mn-MCM-48 and Mn-MCM-L. *J Chem Soc Chem Comm*. 1995;875–876.
27. Jyothi D, Deshpande P, Venugopal B, Chandrasekaran S, Madras G. Transition metal oxide loaded MCM catalysts for photocatalytic degradation of dyes. *J Chem Sci*. doi:10.1007/s12039-011-0148-6.
28. Czechura K, Sayari A. Synthesis of MCM-48 silica using Gemini surfactant with rigid spacer. *Chem Mater*. 2006;18:4147–4150.
29. Kruk M, Jaroniec M, Yang Y, Sayari A. Determination of lamellar phase content in MCM-41 using X-ray diffraction, nitrogen adsorption, and thermogravimetry. *J Phys Chem B*. 2000;104:1581–1989.
30. Luan Z, He H, Zhau W, Klinowski J. Transformation of lamellar silicate into the mesoporous molecular sieve. *J Chem Soc Faraday Trans*. 1998;94:979–983.
31. Yuan Z-Y, Chen T-H, Wang J-Z, Li H-X. Synthesis of mesostructured lamellar aluminophosphates in the presence of alkylpyridinium cationic surfactant. *Mater Chem Phys*. 2001;68:110–118.
32. Zhang C, He H, Tanaka K-i. Perfect catalytic oxidation of formaldehyde over a Pt/TiO_2 catalyst at room temperature. *Catal Commun*. 2005;6:211–214.
33. Tidahy HL, Hosseni M, Siffert S, Cousin R, Lamonier J-F, Aboukaıs A, Su B-L, Giraudon J-M, Leclercq G. Nanostructured macro-mesoporous zirconia impregnated by noble metal for catalytic total oxidation of toluene. *Catal Today*. 2008;137:335–339.
34. Costa LOO, Vasconcelos SMR, Pinto AL, Silva AM, Mattos LV, Noronha FB, Borges LEP. Rh/CeO_2 catalyst preparation and characterization for hydrogen production from ethanol partial oxidation. *J Mater Sci*. 2008;43:440–449.
35. Deshpande PA, Hegde MS, Madras G. Pd and Pt ions as highly active species for the water-gas shift reaction over combustion synthesized zirconia and zirconia-modified ceria. *Appl Catal B Environ*. 2010;96:83–93.
36. Schumacher K, Ravikovitch PI, Chesne AD, Neimark AV, Unger KK. Characterization of MCM-48 materials. *Langmuir*. 2000;16:4648–4654.
37. Schumacher K, Grun M, Unger KK. Novel synthesis of spherical MCM-48. *Microp Mesop Mater*. 1999;27:201–206.
38. Lind A, von Hohenesche CF, Smått JH, Linden M, Unger KK. Spherical silica agglomerates possessing hierarchical porosity prepared by spray drying of MCM-41 and MCM-48 nanospheres. *Microp Mesop Mater*. 2003;66:219–227.
39. Petitto C, Galarneau A, Driole M-F, Chiche B, Alonso B, Di Renzo F, Fajula F. Synthesis of discrete micrometer-sized spherical particles of MCM-48. *Chem Mater*. 2005;17:2120–2130.
40. Liu C, Wang S, Rong Z, Wang X, Gu G, Sun W. Synthesis of structurally stable MCM-48 using mixed surfactants as co-template and adsorption of vitamin B12 on the mesoporous MCM-48. *J Non-Cryst Solids*. 2010;365:1246–1251.
41. Jang HT, Park YK, Ko YS, Lee JY, Margandan B. Highly siliceous MCM-48 from rice husk ash for CO_2 adsorption. *Int J Greenhouse Gas Control*. 2009;3:545–549.
42. Vetrivel S, Pandurangan A. Supported metal oxide catalysts: Their activity to vapor phase oxidation of ethylbenzene. *Ind Eng Chem Res*. 2005;44:692–701.
43. Xia Q-H, Su K-X, Ma X-T, Ge H-Q, Zhu H-B. Efficiently tailoring the pore diameter of mesoporous MCM-48 to micropore. *Mater Lett*. 2005;59:2110–2114.
44. Lazaridis NK, Kyzas GZ, Vassiliou AA, Bikiaris DN. Chitosan derivatives as biosorbents for basic dyes. *Langmuir*. 2007;23:7634–7643.
45. Kennedy Oubagaranadin JU, Murthy ZVP. Characterization and use of acid-activated montmorillonite-illite type clay for lead (II) removal. *AIChE J*. 2010;56:2312–2322.
46. Mellah A, Chegrouche S, Barkat M. The removal of uranium(VI) from aqueous solutions onto activated carbon: Kinetic and thermodynamic investigations *J Colloid Interface Sci*. 2006;296:434–441.
47. Duran C, Ozdes D, Gundogdu A, Senturk HB. Kinetics and isotherm analysis of basic dyes adsorption onto almond shell (*Prunus dulcis*) as a low cost adsorbent. *J Chem Eng Data*. 2011;56:2136–2147.
48. Wong YC, Szeto YS, Cheung WH, McKay G. Equilibrium studies for acid dye adsorption onto chitosan. *Langmuir*. 2003;19:7888–7894.
49. Ho YS, Porter JF, McKay G. Equilibrium isotherm studies for the sorption of divalent metal ions onto peat: Copper, nickel and lead single component systems. *Water Air Soil Pollut*. 2002;141:1–33.

Manuscript received Oct. 8, 2011, and revision received Dec. 1, 2011.